HHS Public Access

Author manuscript

*Nat Mater*. Author manuscript; available in PMC 2024 July 01.

Published in final edited form as:

*Nat Mater*. 2023 July ; 22(7): 913–924. doi:10.1038/s41563-023-01578-1.

# Compressive forces stabilize microtubules in living cells

**Yuhui Li**[1,2], **Ondřej Kučera**[1,2,3], **Damien Cuvelier**[4,5,6], **David M. Rutkowski**[7], **Mathieu Deygas**[4,5], **Dipti Rai**[8], **Tonja Pavlovič**[8], **Filipe Nunes Vicente**[9], **Matthieu Piel**[4,5], **Grégory Giannone**[9], **Dimitrios Vavylonis**[7], **Anna Akhmanova**[8], **Laurent Blanchoin**[1,2], **Manuel Théry**[1,2]

[1]Univ. Paris, INSERM, CEA, UMRS1160, Institut de Recherche Saint Louis, CytoMorpho Lab, Hôpital Saint Louis, Paris, France.

[2]Univ. Grenoble-Alpes, CEA, CNRS, INRA, Interdisciplinary Research Institute of Grenoble, Laboratoire de Phyiologie Cellulaire & Végétale, CytoMorpho Lab, Grenoble, France.

[3]Department of Engineering Technology, South East Technological University, Waterford, Ireland.

[4]Institut Curie, UMR144, Paris, France.

[5]Institut Pierre-Gilles de Gennes, Paris, France.

[6]Sorbonne Université, , F-75005, Paris, France.

[7]Department of Physics, Lehigh University, Bethlehem, PA, USA.

[8]Cell Biology, Neurobiology and Biophysics, Department of Biology, Faculty of Science, Utrecht University, Utrecht, The Netherlands.

[9]University Bordeaux, CNRS, Interdisciplinary Institute for Neuroscience, IINS, UMR 5297, Bordeaux, France.

## Abstract

Microtubules are cytoskeleton components with unique mechanical and dynamic properties. They are rigid polymers that alternate phases of growth and shrinkage. Nonetheless, the cells can display a subset of stable microtubules, but it is unclear whether microtubule dynamics and mechanical properties are related. Recent in vitro studies suggest that microtubules have mechano-responsive properties, being able to stabilize their lattice by self-repair on physical damage. Here we study how microtubules respond to cycles of compressive forces in living cells and find that



**Correspondence and requests for materials** should be addressed to Laurent Blanchoin or Manuel Théry. laurent.blanchoin@cea.fr; manuel.thery@cea.fr.

Author contributions

Y.L., M.T. and L.B. conceived the study and designed the overall experiments. Y.L., D.R. and F.N.V. conducted the experiments. D.C., M.D., T.P., M.P., G.G., D.V. and A.A. provided the materials and shared the methods. Y.L., O.K. and D.M.R. analysed the data. Y.L., M.T. and L.B. wrote the Article. All the authors reviewed, edited and approved the paper.

Additional information

**Supplementary information** The online version contains supplementary material available at https://doi.org/10.1038/s41563-023-01578-1.

**Peer review information** *Nature Materials* thanks the anonymous reviewers for their contribution to the peer review of this work.

Competing interests

The authors declare no competing interests.

microtubules become distorted, less dynamic and more stable. This mechano-stabilization depends on CLASP2, which relocates from the end to the deformed shaft of microtubules. This process seems to be instrumental for cell migration in confined spaces. Overall, these results demonstrate that microtubules in living cells have mechano-responsive properties that allow them to resist and even counteract the forces to which they are subjected, being a central mediator of cellular mechano-responses.

Mechanical forces not only deform cells but also instruct them and therefore regulate the functional organization of tissues[1]. Numerous morphogenetic processes are associated with the reorganization of the microtubule (MT) network and, in particular, to its local stabilization in specific subcellular regions[2], suggesting that MTs adapt to mechanical forces. In addition, several mutant phenotypes in plants and animal cells suggested that MTs could act as mechano-sensors[3]. However, it is not yet known how MTs sense and respond to mechanical forces and how this process could impact MT stability. Indeed, MTs are characterized by fairly particular mechanical and dynamic properties.

Mechanically, MTs are rigid tubes with a high bending stiffness compared with other cytoskeleton polymers[4]. Their persistent length is much longer than the size of the cell, so they grow almost in a straight line throughout the cytoplasm. They are pressurized by their growth against the cell membrane[5]. Interestingly, their embedding in the actin network constrains their buckling under compression, forcing them to adopt short-wavelength bending modes[6]. These high local strains make them well suited to act as sensitive sensors of compressive forces, a possibility that has not yet been investigated.

From the dynamic point of view, MTs are unstable. They rapidly grow by tubulin polymerization at their ends, but whenever their growth is interrupted, they undergo rapid depolymerization[7]. In cells, the instability of MT-growing ends is modulated by end-binding proteins[8]. Among the numerous plus-end-binding proteins, the family of CLIP-associated proteins has been shown to secure end elongation and even rescue MT depolymerization[9]. Interestingly, it has long been observed that one subset of MTs, often more curved than the others, is also more stable. These MTs display more post-translational modifications (PTMs), and they can resist the sequestration of free tubulin dimers without depolymerizing[10]. How certain MTs can be selectively stabilized and the potential role of end-binding proteins in this process are critical but unresolved questions.

Whether and how MT's mechanical and dynamic properties are related is poorly characterized. Tensile forces were shown to stimulate and orient MT outgrowth[11,12]. Compressive forces exerted on the ends of growing MTs in vitro induce the depolymerization of MTs[13]. However, in cells, biochemical signalling from focal adhesions under contractile forces has been shown to stabilize MTs[14,15]. Hence, the direct role of mechanical forces on MTs in cells remains unclear, and their potential role as mechano-sensors and mechano-transducers lacks in-depth characterization.

Recent studies on isolated MTs in vitro have shown that bending forces have an impact on the MT structure, composition and extended lifespan[16–18], suggesting that in a cellular context, MTs may also have specific mechano-responsive properties. However, direct

evidence in living cells has been lacking, and the impact of mechanical forces on MT stability in vivo has not yet been investigated. Here we tested the mechano-responsive properties of MTs in cells by submitting them to various sorts of mechanical forces and analysing the impact on MT dynamics.

## MT deformation and reorganization by compressive forces

We applied controlled mechanical forces to retinal pigment epithelial (RPE1) cells to test the response of the MT network. We used a thin silicone sheet clamped to a motorized stage to apply stretch and compression cycles (SCC) to cells[19] (Supplementary Fig. 1a–c and Supplementary Video 1). We implemented a method to print adhesive micropatterns on the silicone sheet to normalize the response of the cells and to study the cytoskeleton response independent of the resultant cell-shape change (Fig. 1a and Supplementary Fig. 1d,e). The shape of the silicone sheet and its clamping in the movable elements ensured a uniaxial SCC without compensation by perpendicular compression in the central part (Supplementary Fig. 2). We first tested the resistance of RPE1 cells to the deformation by applying SCC of different magnitudes (10–60%). The cells detached at 40%, but there was no visible impact on the shape of the cell at 10% strain (Supplementary Fig. 3a,b). We also tested the effect of SCC frequency on cell detachment. The cells started to detach at 1.0 Hz but held up well to 10% strain cycles at 0.1 Hz (Supplementary Fig. 3c,d). We, therefore, chose to constrain the cells by applying 10 cycles of 10% SCC for 2 min (that is, 0.08 Hz).

The MT network resisted the SCC and remained globally isotropic despite a few stereotypical changes (Fig. 1b; Supplementary Fig. 3e,f provides more examples). In particular, we noticed the appearance of curved MTs along the cell periphery (Fig. 1c). Indeed, the measurement of the local orientation of MTs and the characteristic wavelength (Fig. 1d) revealed an increase in orientation variations (Fig. 1e) and a shortening in the characteristic wavelength (Fig. 1f) in sections along the SCC axis. These results suggest that the limited longitudinal elasticity of MTs does not allow them to expand during stretching phases, but that friction with the surrounding cytoplasm promotes their bending with a short wavelength during compression phases[6]. As previous reports have shown an interesting correlation between the curvature, stiffness and stability of MTs[10,20], we next tested whether SCC has an impact on MT stability.

## Compressive forces stabilize MTs

Nocodazole (NZ) is a cell-permeable drug that binds to tubulin dimers and thus triggers the disassembly of dynamic MTs[21]. We, therefore, measured the stability of MTs by testing their resistance to low doses of NZ and compared unstressed cells with those subjected to SCC (Fig. 1g). Interestingly, SCC had no impact on the overall density of MT (Fig. 1h, −NZ). However, it drastically increased the amount of MTs that could withstand NZ (Fig. 1h, +NZ). This mechano-induced resistance to the sequestering of tubulin dimers could also be observed in the epithelial kidney cell line PtK2 and the myoblast cell line C2C12 (Supplementary Fig. 4). To further characterize the MT dynamics, we analysed the binding of EB1 to the plus ends of MTs since its local accumulation is a faithful indicator of MT growth[8]. EB1-positive comets at the plus ends of MTs appeared shorter and less

numerous after SCC (Fig. 1i,j). Interestingly, additional EB1-positive spots appeared along the MT shaft, at some distance from the end (Fig. 1k). In addition, the use of a stretching device composed of a thin stretchable silicone layer sliding over a glass surface allowed live imaging after SCC[22]. It revealed that EB1 comets moved more slowly (Fig. 1l and Supplementary Video 2) and had a longer lifetime (Fig. 1m), indicating that MT growth was reduced. Both sets of data showed that SCC had a strong stabilizing effect on MTs.

It should be noted that SCC has a well-characterized effect on the reorientation of actin filament bundles along the SCC axis at short timescales (several minutes) and along the minimum strain axis at longer timescales (several hours) in response to a wide range of frequencies (mHz to Hz)[19,23,24]. As the actin network also influences MT stability, the stabilization of MTs along the SCC axis that we observed might be due to a reorganization of the actin network. In our conditions of frequency and strain, most actin bundles were destroyed by SCC (Supplementary Fig. 5a)[25]. However, consistent with the role of the actin network in resisting MT buckling under pressure[6], we could clearly observe the alignment of actin filaments along the MTs that were deformed by SCC (Supplementary Fig. 5b,c). In addition, larger bundles were not observed in response to NZ treatment as they were in non-stretched and compressed cells (Supplementary Fig. 5d). The possible role of these actin filaments in response to SCC was further assessed by treating the cells with cytochalasin D to induce actin network disassembly. This treatment did not affect the amount of NZ-resistant MTs (Supplementary Fig. 5e,f), confirming that MT stabilization was not a consequence of actin filament alignment with curved MTs or actin bundles destruction but rather an intrinsic property of MTs.

## MT mechano-stabilization in enucleated cells

The interaction of MTs with the nucleus could also be involved in their stabilization. Indeed, the nucleus is a major load-bearing structure in cells[26]. Since it interacts with MTs[27], its deformation by SCC may have an indirect impact on MT stability. Therefore, we tested whether the shape of the nucleus was affected in our SCC range. We found that the nuclei appeared elongated along the SCC axis (Supplementary Fig. 6a–c), suggesting that they undergo a non-elastic deformation in response to SCC. The nucleus volume was not affected by stretching (Supplementary Fig. 6d,e). To challenge this hypothesis of an indirect role of the nucleus and to further assess the specific response of the MTs to SCC, we enucleated the cells by centrifugation and plated the resulting cytoplasts onto micropatterns on stretchable membranes[28].

Cytoplasts appear to be more resistant to SCC than cells (Supplementary Fig. 6f). However, strain larger than 20% seems to induce some fragmentation of the MT network (Supplementary Fig. 6g), so we decided to stimulate the cytoplasts to the same level as cells, that is, 10%. Interestingly, the reorientation and deformation of MTs by SCC were more pronounced in cytoplasts than in cells. The entire network architecture was impacted (Supplementary Fig. 7). We analysed the orientation of MTs with respect to the cytoplast radius. To that end, we applied a geometric transformation, which maps radial and angular lines onto the orthogonal grid, to the fluorescent images of MTs (Fig. 2a,b). Then, we measured the angular distribution of MTs in those transformed images (Fig. 2c). This

analysis showed that MTs have reoriented from a rather radial to a circular organization, as revealed by their reorientation from the vertical to the horizontal direction in the curvi-linear reference (Fig. 2c). We also analysed the local variations in MT orientation with respect to the curvi-linear axis (Fig. 2d) and found that sections of MTs that were aligned with the SCC axis (azimuth angle between 45° and 90°) were more curved (Fig. 2d,e). Furthermore, the proportion of NZ-resistant MTs was significantly increased by mechanical SCC (Fig. 2f,g and Supplementary Fig. 7). The average density of NZ-resistant MTs was about five times higher in cytoplasts subjected to SCC than in untreated cytoplasts. As in the case of cells, mechanically induced stable MTs tended to align with the SCC axis (Fig. 2h). These results show that the stabilization of MTs by SCC was independent of nucleus deformation and probably a specific response of MTs to external stretch–compression forces.

## MT mechano-stabilization is progressive

To better characterize the mechano-stabilization of MTs by SCC, we measured its dependency on the number of SCC and its duration. Cytoplasts were subjected to an increasing number of SCC (12 s each) and then treated with NZ to assess the amount of stable MTs (Fig. 3a). The effect was progressive and the total length of stable MTs was almost proportional to the number of SCC (Fig. 3b,c). We then subjected the cytoplasts to 10 SCC in 2 min and waited for increasing delays from 0 to 60 min before treating them with NZ (Fig. 3d). We found that the stabilization lasted for at least 10 min, decreased after 30 min and went back to the basal level of unsolicited cytoplasts after 1 h (Fig. 3e,f).

## Relocalization of plus-tip proteins by compression forces

We then investigated the mechanism supporting the mechano-stabilization effect. MT stability is often correlated with PTMs of tubulins[20,29]. We, therefore, wondered whether the mechanical stabilization we observed was associated with PTMs. We measured the amount of detyrosinated and acetylated tubulin (Supplementary Fig. 8a,b) and found no effect of SCC. We observed the orientation of acetylated MTs before and after SCC to test whether they were more specifically stabilized by SCC, but we found no difference (Supplementary Fig. 8c,d). These observations showed that stabilization was not a consequence of PTMs of tubulins but rather mediated by another pathway. In particular, the tortuous shape of NZ-resistant MTs suggests that their stabilization could arise from local deformation rather than end stabilization. Furthermore, the relocalization of EB1 along the length of MTs in cells subjected to SCC (Fig. 1k) suggests that stabilization may be associated with the protective role of plus-tip complexes acting on the lattice of the MTs[30,31].

We tested this possibility and analysed the spatial distribution of EB1 in cytoplasts (Fig. 4a). Consistent with the experiments in cells, EB1 was localized to the growing ends of MTs under control conditions and along the entire length of MTs in response to SCC (Fig. 4b). We also analysed the localization of CLASP2, which is a plus-end-binding protein that also decorates the entire lattice of MTs localized at the front of migrating cells[32], and plays a protective role on the damaged lattice of MTs in vitro[31]. As for EB1, it relocated from the MT ends to the MT shaft in response to SCC (Fig. 4c,d). To more precisely analyse this relocalization process, we implemented an image segmentation tool to quantify this

effect (Methods). It allowed us to skeletonize MTs[33] and detect CLASP spots to measure the ratio between CLASP bound to MT versus cytoplasmic CLASP signal (Supplementary Fig. 9). This analysis revealed the clear recruitment of CLASP2 along the length of MTs in response to SCC (Fig. 4e), particularly on the curved regions of MTs (Fig. 4f). Furthermore, NZ-resistant MTs also showed a higher density of CLASP2 compared with the entire pool of MTs (Fig. 4e), and this density was enriched by SCC (Fig. 4f and Supplementary Fig. 9b). In addition, heat maps of the entire cytoplasts revealed a clear correlation between the MT-associated CLASP2 and regions where the MT orientations were highly variable (Supplementary Fig. 9c). Overall, these results showed that CLASP2 was enriched on MTs that were bent by external forces and became resistant to NZ (Fig. 4g).

## CLASP2 supports MT mechano-stabilization

CLASP2 is a well-known regulator of MT plus-end growth[34,35]. Here its localization suggests that it could stabilize MTs by binding to regions that have been bent by mechanical forces. This possibility could be directly tested by removing the two alleles coding for CLASP2 with CRISPR–Cas9 (Methods). The absence of CLASP2 was then tested by western blotting (Fig. 5a) and by immunostaining in fixed cells (Fig. 5b). Surprisingly, we detected no impact of the absence of CLASP2 on the total amount of MTs or on the amount of NZ-resistant MTs in SCC-untreated cytoplasts (Fig. 5c), suggesting that CLASP1 may have compensated for the loss of CLASP2 (ref. 36). However, the absence of CLASP2 had a striking effect on SCC-treated cytoplasts, in which it completely abolished the mechano-stabilization of MTs (Fig. 5d). The specificity of this effect was tested by overexpressing GFP-CLASP2 in CLASP2 knockout (KO) cells, which was sufficient to almost double the amount of NZ-resistant MTs in SCC-treated cytoplasts (Fig. 5e). We have, thus, demonstrated that CLASP2 has a direct and specific effect on the stabilization of MTs in response to mechanical forces.

## MT mechano-stabilization promotes cell migration

Finally, we investigated whether our previous observations can be generalized to forces that were not imposed by the experimenter but by the cells themselves during their migration. The cells are able to migrate through tiny constrictions by compressing their nuclei[37]. We tested whether the constraints exerted by these constrictions on the cells had an impact on MT stability. The cells were enclosed in 12-μm-wide microfabricated channels along some of which the cells encountered 4-μm-wide constrictions (Fig. 6a and Supplementary Fig. 10). We tested the impact of cell self-deformation as they passed the constriction on MT stability by subjecting them to the NZ treatment we used previously. We found that cells migrating in channels with constriction had more NZ-resistant MTs (Fig. 6b,c). Furthermore, the density of those NZ-resistant MTs was higher in the front part of the cells that have passed the constriction than in the back of the cell (Fig. 6d). As for cells subjected to SCC, we further assessed the MT stability by looking at the localization of plus-tip proteins. We found that EB3-positive comets slowed down in the part of the cells that passed the constriction (Fig. 6e,f and Supplementary Video 3) and that EB1 relocalized from ends to the entire shaft of the MTs after the constriction (Fig. 6g). In addition, the

CLASP2 density per MT increased in the cell part that passed the constriction (Fig. 6h,i). All these observations were reminiscent of our characterization of cells subjected to SCC.

These results prompted us to test the role of CLASP2 in the stabilization of MTs as cells migrate through constrictions. We studied the migration of CLASP2 KO cells in straight and constricted channels. A NZ resistance assay showed us that MTs were no longer stabilized in mutant cells passing the constriction (Fig. 6j,k). As expected from previous works[35], the migration of CLASP2 KO cells was generally impaired although not completely blocked, as shown by their reduced velocity in straight channels (Fig. 6l; average speed, 7.2 μm $h^{-1}$ for wild type (WT) versus 4.8 μm $h^{-1}$ for CLASP2 KO). But the effect was particularly striking in constricted channels. In CLASP2 KO cells, MTs were no longer stabilized at the constriction and the cells tended to retract (Supplementary Video 4). Indeed, most mutant cells could not pass the constriction (Fig. 6m): 74.0% ± 3.0% of WT cells ($n$ = 285) passed the constrictions in the 9 h that our observation lasted, whereas only 15.5% ± 3.0% of CLASP2 KO cells ($n$ = 107) managed to pass (Supplementary Video 5). Since CLASP2 and EB1 relocalized to MTs that have passed the constrictions and that CLASP2 was necessary for the specific stabilization of MTs at these constrictions, these results suggest that the migration was impaired not only by the deficient stabilization of plus ends by CLASP2 but also by its absence of relocalization along the length of MTs that were subjected to compressive forces as they passed through the constriction.

## Outlook

In this study, we demonstrated that MTs are mechano-responsive in living cells. We found that SCC can tear up the actin network and stabilize MTs. Interestingly, our results show that MT stabilization depends on CLASP2, which relocates from the tip to the shaft of MTs that have been bent by compressive forces (Fig. 4f). This effect probably explains the stability of MTs at the front of the migrating cells that are subjected to compressive forces by the rearward flow of the actin network and that are fully decorated with CLASP[32]. Overall, these results show that MTs are not rigid rods with a dynamic biochemical exchange only at the ends but that their entire shaft is active[38], responding to mechanical forces by deforming and consequently recruiting biochemical signals locally. The stabilization of compressed MTs could explain the correlation between MT curvature and stability[10,20,39,40]. It might also account for the selective stabilization of a subset of MTs in cells since only compressed MTs would be stabilized. This mechanism can explain how cells polarize specifically towards regions where they are mechanically stressed, such as wounds[41].

The MT mechano-stabilization process also probably contributes to the general cell response to compressive forces and to the adaptation of cell architectures in compressed tissues[42]. In particular, stable MTs are present in beating adult cardiomyocytes, where they undergo compression. However, the mechanism relating MT stability to cardiomyocyte contractility is still unclear[43]. Our results on myoblasts suggest that the SCC, such as those associated with a heartbeat, are sufficient to stabilize MTs. In turn, tubulin PTMs, which occur on long-lived MTs, have been shown to impact cardiomyocyte contractility[44], and interfering with these modifications of stable MTs is currently a promising strategy to reduce the resistance of stable MTs to cardiomyocyte contraction[45]. Thus, our identification of CLASP2 as a

master regulator of MT mechano-stabilization may open up new strategies for the treatment of cardiomyopathies.

Mechanical compression has also recently been recognized as a key regulator of cell physiology. Spatial confinement provides physical boundaries that cells can use to produce pushing forces and migrate forward[46]. But compressive forces also impact signalling pathways, gene expression and cell fate in ways that are much less understood. In particular, pressure negatively regulates cell cycle progression and tumour growth[47,48] but promotes cancer cell invasion[49]. MT stability is also tightly associated with cell differentiation[50] and directed cell migration[41]. The mechano-stabilization of MTs might, thus, be an interesting mediator of the broad impact of compressive forces on cell physiology.

## Online content

Any methods, additional references, Nature Portfolio reporting summaries, source data, extended data, supplementary information, acknowledgements, peer review information; details of author contributions and competing interests; and statements of data and code availability are available at https://doi.org/10.1038/s41563-023-01578-1.

## Methods

### Preparation of micropatterned silicone sheet

The micropatterning of cells on a silicone sheet was performed according to a deep-ultraviolet (UV) method previously described in the literature[25,51]. Briefly, silicone substrate (PF-40-X4, Gel-Pak), whose thickness is 170 μm and Young's modulus is about 500 kPa (ref. 52) was washed with 75% ethanol for 5 min on a rotator at 30 oscillations $min^{-1}$ and then incubated with 0.5 mg $ml^{-1}$ poly(L-lysine)-*graft*-poly(ethyl ene glycol) (PLL-*g*-PEG) (no. ZZ241PO22, JenKem Technology) in 10 mM HEPES buffer (pH 8.6) for 3 h at room temperature. After drying, the modified silicone samples were stored at 4 °C for at least 1 h. Next, the PLL-*g*-PEG side of the silicone substrate was placed on a synthetic quartz photomask bearing a disc shape of 50 μm in diameter. The PLL-*g*-PEG layer of the silicone membrane was exposed to deep-UV ($\lambda$ = 190 nm) through the non-chromed windows of the photomask using UVO-Cleaner (model no. 342A-220, Jelight), at a distance of 5 cm from the UV lamp with a power of 6 mW $cm^{-2}$ for 5 min. The silicone sheet was then gently peeled off the mask and incubated with 10 μg $ml^{-1}$ fibronectin from bovine plasma (no. F1141, Sigma-Aldrich) in 10 mM HEPES buffer (pH 8.6) for 20 min at room temperature. For micropattern imaging, a silicone substrate was incubated with a mix of 10 μg $ml^{-1}$ fibronectin and 10 μg $ml^{-1}$ fibrinogen–Alexa Fluor 546 conjugate (no. F13192, Invitrogen, Thermo Fisher Scientific) in 10 mM HEPES buffer (pH 8.6) for 20 min at room temperature. Then, the silicone substrates were rinsed three times with phosphate-buffered saline (PBS). Before plating the cells, the micropatterned samples were stored in PBS at 4 °C overnight.

### SCC

To enable uniaxial SCC to the micropatterned cells, we developed an automatic stretcher combined with either a piezoelectric motor (M-663, 18 mm, linear encoder, 0.1 μm resolution, Physik Instrumente) or a mechanical motor (M-110.1DG, 25 mm, linear encoder,

0.1 μm resolution, Physik Instrumente)[25]. First, the silicone grease was exposed to UV light for 1 h in an ultraclean workbench (GE Bayer Silicones) and then plated on top of the micropatterned silicone sheet (35 mm × 15 mm) to generate a compartment for the culture medium. Second, the silicone sheet was mounted on the stretcher consisting of a fixed (holding) arm and a mobile (stretching) arm connected to the mechanical motor. Then, cyclic uniaxial stretches with variable strains (from 10% to 60%) and frequencies (0.08, 0.10 or 1.00 Hz) were applied. To make the SCC assay compatible with confocal microscopy, we also used another micromechanical device described previously[22]. Briefly, we deposited an ultrathin polydimethylsiloxane (PDMS, 10 μm in thickness, 10/1 w/w PDMS A/crosslinker B, SYLGARD-184, Dow Corning) on a lubricated glass coverslip to allow simultaneous membrane stretching and ensure planarity during deformation. To handle such a thin PDMS substrate and avoid mechanical distortion, we enhanced its mechanical stability by adding a thicker (40 μm) elastomeric frame (PF-40-X0, Gel-Pak) on top of the thin PDMS layer, keeping the size of the observation chamber as small as possible (3 mm × 3 mm, that is, 9 $mm^2$). Next, low-viscous glycerol (glycerol for fluorescence microscopy; CAS 56–81-5, Merck) was spun on a plasma-cleaned glass coverslip to allow sliding between the PDMS membrane and the glass coverslip and then sandwiched with the plasma-cleaned PDMS sheet, creating a glycerol layer of ~0.7 μm thickness. Finally, the glass–PDMS sandwich was assembled with a three-dimensionally printed microdevice. The micromechanical device was connected to a piezoelectric motor (M-663, Physik Instrumente) positioned on opposite sides of the observation chamber on the PDMS frame. The observation chamber or the whole microchip could be filled with the culture or observation medium.

## Mechanical characterization of the SCC device

We numerically and experimentally tested the mechanical properties of the SCC device. As one intrinsic characteristic of uniaxial stretching is that the substrate is stretched along the deformation axis and can be compressed perpendicularly to it, which can be amplified by boundary effects, we wanted to check whether our device allows obtaining a controlled and homogeneous deformation over the observation region. Therefore, we first simulated the surface deformation fields for a defined percentage (5%, 10% and 20%) of stretch using finite element simulation software (COMSOL Multiphysics 4.0a). The boundary conditions were consistent with the dimensions of the stretching device, and the silicone substrate was treated as an isotropic, neo-Hookian material with an elastic modulus derived from previous work. Our simulation results showed that the surface strain fields in the central observation chamber should be remarkably uniform and uniaxial, up to 20% stretch. To experimentally characterize the surface strain fields of the silicone sheet under stretch (20%), mesh grids were marked on the sample. The resulting deformation map is also homogeneous and corresponds well with the simulation data. Then, to clarify the SCC amplitude over time, we plated red fluorescent beads (1 μm in diameter; R0100, Thermo Fisher Scientific) on the top surface of silicone sheets and tracked the bead motion after a tiny stretch cycle (2%, 0.05 Hz).

## Cell culture and seeding

Human-telomerase-immortalized RPE1 cells (ATCC), WT RPE1 cells, CLASP2 KO cells, GFP-EB1 and GFP-EB3 expressing RPE1 cells were cultured in Dulbecco’s modified

Eagle's medium with nutrient mixture F-12 (DMEM/F-12; no. 31331093, Gibco, Thermo Fisher Scientific) supplemented with 10% foetal bovine serum (no. 10270106, Gibco, Thermo Fisher Scientific) and 1% penicillin and streptomycin in a humidified incubator at 37 °C and 5% $CO_2$. C2C12 (myoblasts) (ECACC, Sigma-Aldrich) and Ptk2 cells (ATCC) were cultured in DMEM with GlutaMAX (no. 31966021, Gibco, Thermo Fisher Scientific) supplemented with 10% foetal bovine serum and 1% penicillin and streptomycin in a humidified incubator at 37 °C and 5% $CO_2$. For myotube generation, DMEM with 2% horse serum (no. S2700500, Biowest) was added to the Petri dish instead of the initial culture medium after 24 h of culture. Cells were detached with TrypLE (no. 12605036, Gibco, Thermo Fisher Scientific), centrifuged and resuspended in a complete medium at $2 \times 10^4$ cells $ml^{-1}$. Cells were plated on the patterned silicone substrate and allowed to spread for 1 h before washing the unattached cells with a prewarmed complete medium. The cells were incubated with a fresh culture medium for at least 1 h at 37 °C to promote correct spreading and polarization before further treatments. The same culture and plating procedure was applied to the cytoplasts.

## Enucleation of cells

RINZL plastic coverslides were treated with 1 μg $ml^{-1}$ fibronectin and 12 μg $ml^{-1}$ collagen I from rat tail (no. A1048301, Gibco, Thermo Fisher Scientific) for 1 h. The cells were then plated on plastic slides (no. 7189001, Electron Microscopy Sciences) and incubated overnight to achieve 80% confluence. To remove the nuclei from the cells, two plastic slides were placed in a 50 ml tube (no. 357007, Beckman Coulter) resistant to high-speed centrifugation in a complete medium supplemented with 5.9 μM cytochalasin D (no. C8273, Sigma-Aldrich) for 30 min at 37 °C and then centrifuged at 15,000×*g* for 1 h at 37 °C. The enucleated cells were subsequently washed twice with prewarm DMEM/F-12 and incubated for 30 min at 37 °C before being seeded on micropatterned silicone substrates.

## Drug treatment

MTs were disassembled by incubating cells/cytoplasts with 2 μM NZ (no. M1404, Sigma-Aldrich) for 15 min (for cells) or 10 μM for 30 min (for cytoplasts) until fixation. Actin filaments were disassembled by incubating cells with 0.1 μM cytochalasin D for 20 min. As a control, 0.1% dimethyl sulfoxide (the solvent for either NZ or cytochalasin D) was added to the cultures.

## Microchannel fabrication and cell loading

Microchannels were fabricated according to earlier work[37]. Briefly, PDMS (10/1 w/w PDMS A/crosslinker B) was used to prepare 12-μm- or 10-μm-wide and 5-μm-high microchannels with/without constrictions of 15 μm lengths and 4 μm widths from a self-made epoxy mould. Both microchannels and coverslides were treated with plasma for 1 min and then stuck together and placed in an oven at 70 °C for 10 min. Then, the stick chips were treated with a vacuum for 10 min and plasma for 1 min, respectively. Channels were then incubated with 10 μg $ml^{-1}$ fibronectin for 30 min and rinsed with PBS at least three times and finally incubated with a culture medium for at least 3 h before loading the cells. The cells were centrifuged and resuspended in a complete medium at $5 \times 10^6$ cells $ml^{-1}$ and then 5 μl suspension was plated in each chamber of the microchannels.

### Antibodies, IF and immunoblotting

We used rabbit monoclonal antibodies against α-tubulin (no. ab52866, Abcam), monoclonal mouse antibodies against β-tubulin (no. T4026, Sigma-Aldrich), monoclonal mouse antibodies against acetylated tubulin (no. MABT868, Sigma-Aldrich), polyclonal rabbit antibodies against detyrosinated tubulin (a gift from M.-J. Moutin[53]), monoclonal mouse antibodies against EB1 (no. 610534, BD Biosciences), monoclonal rat monoclonal antibodies against CLASP2 (no. KT68, Absea) and phalloidin-stabilized actin (fluorescein isothiocyanate labelled; no. P5282, Sigma-Aldrich). Primary antibodies were diluted for immunofluorescence (IF) as follows: α-tubulin (1:500), β-tubulin (1:500), acetylated tubulin (1:5,000), dTyr tubulin (1:1,000), EB1 (1:2,000), CLASP2 (1:500) and actin (1:500). Secondary antibodies were diluted for IF as follows: Alexa Fluor 555 goat anti-rat (1:500; no. A21434, Invitrogen, Thermo Fisher Scientific), Alexa Fluor 488 donkey anti-mouse (1:500; no. A21202, Invitrogen, Thermo Fisher Scientific), Alexa Fluor 488 goat anti-rabbit (1:500; no. A11008, Invitrogen, Thermo Fisher Scientific) and Alexa Fluor 546 goat anti-rabbit (1:500; no. A11010, Invitrogen, Thermo Fisher Scientific). Primary antibodies were diluted for immunoblotting as follows: β-tubulin (1:5,000) and CLASP2 (1:5,000). Secondary antibodies were diluted for immunoblotting as follows: IRDye 680LT goat anti-rat and IRDye 800CW goat anti-mouse (1:5,000; Li-Cor Biosciences).

For MT staining, the cells were prepermeabilized in 0.5% Triton X-100 (no. 2000-C, Euromedex) in a cytoskeleton buffer for 15 s and then fixed in 0.5% glutaraldehyde (no. 00216–30, Polysciences) in a cytoskeleton buffer with 0.5% Triton X-100 and 10.0% sucrose for 15 min at room temperature. The cells were then washed three times with PBS–Tween 0.1% and incubated in a quenching agent of 1 mg $ml^{-1}$ sodium borohydride (no. 452882, Sigma-Aldrich) for 10 min at room temperature. For EB1 or CLASP2 immunostaining, the cells were fixed in cold methanol at −20 °C for 2 min. For all these conditions, after fixation, the cells were washed with PBS–Tween 0.1% and then blocked with 3% bovine serum albumin (no. A7906, Sigma-Aldrich) for 1 h. The cells were incubated with appropriate dilutions of primary antibodies in PBS containing 3.0% bovine serum albumin and 0.1% Tween overnight at 4 °C in a humid chamber. After washing three times with PBS–Tween 0.1%, the PDMS substrates were then incubated with appropriate dilutions of secondary antibodies diluted in PBS containing 3.0% bovine serum albumin and 0.1% for 1 h at room temperature in a humid chamber. After washing three times with PBS–Tween 0.1%, coverslips were then mounted onto slides using ProLong Gold Antifade reagent containing DAPI for nuclei staining (no. P36935, Invitrogen, Thermo Fisher Scientific). The same immunostaining procedure was applied for cytoplasts on the silicone substrate. For cell migration experiments, we used a SiR-tubulin kit (no. SC002, Spirochrome) to label the MTs. Briefly, we diluted the SiR-tubulin stock (1 mM) to 400 nM in a DMEM/F-12 culture medium and incubated the cells for 3–4 h before imaging. Meanwhile, we added 10 μM verapamil (a broad spectrum efflux pump inhibitor) in the medium to improve the staining efficiency.

### Generation of CLASP2 KO cell line using CRISPR–Cas9

A 20-nucleotide guide sequence targeting the exon-encoding part of the TOG2 domain of CLASP2 was designed using the CRISPR design tool (https://www.zlab.bio/resources)

for the following target sequence: 5′-AGCTAAGGATCTTAGATCCCAGG-3′ guide sequence was cloned using BbsI restriction sites of pSpCas9(BB)-2A-Puro (PX459), purchased from Addgene[54]. WT RPE1 cells were transfected with PX459 plasmid containing the corresponding guide sequence for 24 h using FuGENE 6 (Promega). Following 72 h of 4 μM puromycin selection, cells were recovered and isolated for clone selection. Monoclonal CLASP2 KO cell lines were characterized and validated by western blotting and genomic-DNA PCR sequencing using the following primer set. Forward primer, 5′-AGTTTACATTTCTCCGTCGTGC-3′; reverse primer, 5′-ATATGCAACAACACTGCTTAGG-3′. The sequencing results confirmed the generation of a stop codon in the open reading frame due to a frameshift mutation created by the deletion of the 111th bp in exon 11. This led to the translation of only 392 aa residues of CLASP2 (UniProtKB, E7ERI8).

## Cell transfection

GFP-CLASP2 plasmids are cloned from *H. sapiens* and constructed in pEGFP-C1 by linking the 5′ portion of the human truncated EST clone 7k43h10.(IMAGE:3478506) to the nucleotides 194–5,614 of the KIAA0627 cDNA[55]. GFP-CLASP2 plasmids were transfected into cells using an X-tremeGENE kit as per the manufacturer's instructions 48 h before the experiment (XTG9-RO, Sigma-Aldrich). The transfected cells were then put to the enucleation procedure.

## Imaging

Images of the different immunostainings were acquired on a Zeiss LSM880 or LSM900 confocal microscope (Axio Observer) using either a ×63 magnification objective (Plan-Apochromat 63×/1.4 oil) or a ×20 magnification objective (Plan-Apochromat ×20/0.8). Only cells that were well spread out on the disc micropatterns were selected for imaging.

Image acquisition for the time lapse of GFP-EB1/3 RPE1 cells was performed on an inverted microscope (DMi6000, Leica) equipped with a spinning-disc unit CSU-X1 (Yokogawa Electric) through an oil-immersion objective (Leica, HC PL APO ×63/1.40 oil) objective every 1 s during 2 min or 4 min for each time lapse. The setup was equipped with a live-cell chamber, and the temperature was constantly kept at 37 °C. The EB1/3 comets were excited with a 491 nm laser line, and the emission was observed with a standard GFP filter. The microscope was monitored with MetaMorph software (version 7.7.11.0, Universal Imaging). Image acquisition for the time lapse of SiR-tubulin-labelled RPE1 cells was performed on an ECLIPSE Ti-E Nikon inverted microscope equipped with a CSU-X1-A1 Yokogawa confocal head, an Evolve electron-multiplying charge-coupled device camera (Roper Scientific, Princeton Instruments) every second during 14 h. To register the fluorescence images and measure the PDMS deformation, we adsorbed 0.1 μm fluorescent beads (TetraSpeck Microspheres, Thermo Fisher Scientific) on the SCC chamber that were imaged during the entirety of the microscope acquisitions.

## Image analysis

**MT segmentation.—**MTs in cells were segmented using SOAX software (v. 3.7)[33]. Briefly, the underlying SOAX method uses multiple stretching open active contours that

are automatically initialized at image intensity ridges and then stretched along the centre lines of the filaments in the network. The MT density was determined by the ratio of the total number of MTs in individual cells segmented by SOAX and cell spreading area. The total length of MTs in the cells was calculated by summing the length of the SOAX-segmented MTs. The same segmentation analysis was performed for the cytoplasts. For the quantification of small MTs in cytoplasts, the raw data were converted into eight-bit grey-scale images and then analysed with an Image-Pro Plus cluster plug-in (v. 6.0, Media Cybernetics).

**Quantification of cortical MT deformation.—**To quantify the quasi-periodic deformation of cortical MTs on SCC, we analysed their spatial wavelength similar to a previously described method[56]. Briefly, we obtained the orientation of the MTs by evaluating the gradient structure tensor as implemented in the OrientationJ[57] plug-in for Fiji 1.52v (ref. 58). Using a custom MATLAB (v. 2018a, MathWorks) script, with the aid of MATLAB–Fiji interface MIJ[59], we extracted four annulus sectors corresponding to the cortical regions (angular length of each sector was 0.6 rad and the side length was 0.6 μm) from the orientation field. These sectors were paired: one pair corresponding to the cortical part, which did not experience circumferential strain, and the other pair that underwent the maximum circumferential strain during SCC. In these pairs, using fast Fourier transform, we calculated the mean spectrum of orientation along the circumferential direction, which was corrected for discontinuities arising from the modulo operation of the angle assignment. We measured the wavelengths corresponding to the most prominent non-zero mode of the obtained spectra. These wavelengths are due to the linearity of the Fourier transform, equivalent to the principal wavelengths of the MT deformation.

**Geometric transformation of images.—**To facilitate analysis and visualize the MT orientation, we applied a geometric transformation, as shown in Fig. 2a. This conformal mapping transforms a disc into a rectangle in a way that (1) the radial lines become parallel line segments and (2) circles concentric with the disc become line segments, too. The two types of resulting line segments—namely, (1) and (2)—are perpendicular as a result of conformity. The centre of the disc, which can be treated as a circle with zero radius, maps on a line segment similar to other concentric circles. To apply this transformation to the centred images of cells on micropatterns, we used a numerical method written in MATLAB. The fluorescence intensity profiles along the circular path concentric with the cell were sequentially taken with increasing radius. Each profile was filtered using a linear anti-aliasing Finite Impulse Response (FIR) filter and resampled to obtain profiles of identical lengths. The resulting profiles were arranged in a matrix and visualized.

**EB comet tracking and analysis.—**The moving speed and duration time of the EB comets were quantified using the TrackMate plug-in for Fiji[60]. To build the average intensity distribution at the MT growing tip, we generated intensity profiles of a 6-pixel-thick line (200 nm) of 4–5 μm length along the middle axis of the MT at the MT tip using Fiji. The fluorescence profile was then normalized by the maximum intensity value.

**Quantification of orientation variance of MTs.—**To visualize and quantify the variation in MT orientations from all the cytoplasts imaged at a particular experimental condition, we used the variance in MT orientation[61] of the mean projection of MTs. The orientation vector field of MTs was obtained using OrientationJ, as described above. A sliding window was then applied to this field in MATLAB. Within each window position, we calculated the mean resultant length of the orientation unit vectors, $\bar{R} = \frac{1}{N}\left\|\sum_{i=1}^{N} \vec{v}_i\right\|$ and the circular orientation variance as $V = 1 - \bar{R}$. To visualize the result, the matrix of orientation variances was resized using the bicubic interpolation method, and the parts of the field outside the cell were masked by thresholding the original average image.

**Co-localization between MT and CLASP2.—**To determine the coupling state of CLASP2, we used the super-resolution reconstruction of the fluorescence images. MTs were segmented from the 488 nm channel of fluorescence images using SOAX (v. 3.7)[33]. This method extracts the centre lines of MTs, which we interpret as the likeliest estimate of the axes of MTs. The CLASP2 was segmented from the 555 nm fluorescence channel using the FIESTA (v. 1.05) particle tracking software[62], which estimates the positions of the molecules from the two-dimensional Gaussian approximation for the point spread function. Next, we deleted MT and CLASP2 detections that fall within the nuclear region, which we identified by thresholding the fluorescence image in the DAPI channel. The coordinates of the remaining MTs and CLASP2, which we interpret as localized within the cytoplasm, were compared in MATLAB to determine their mutual distances. For each cytoplasmic CLASP2 detection, we calculated the shortest distance to the nearest MT axis. We considered CLASP2 as associated with MT if the particle was confined within the coupling radius from an axis of the MT. This radius was estimated as 40.1 nm from the physical size of the construct of CLASP2 (7.5 nm (ref. 63)), primary and secondary antibodies (20.1 nm (ref. 64)) and MT geometry (radius, 12.5 nm (ref. 65)). Otherwise, CLASP2 was regarded as uncoupled.

**Nuclear volume.—**The nuclear volume was quantified by analysing the *z*-stack confocal images of an individual nucleus using three-dimensional slicer software (v. 5.1). The scaling per pixel is 0.099 × 0.099 × 0.450 μm for each sample. The segmentation and volume calculation were applied by using the segment statistics tool in a three-dimensional slicer.

## Statistical analysis

Statistical analyses were performed using the GraphPad Prism 6 software and RStudio (v. 1.4). The respective numbers of data points, *n*, are indicated in the figure captions. The indicated *P* values were obtained using a two-tailed unpaired non-parametric Mann–Whitney test or Kruskal–Wallis test with Dunn's multiple comparisons test.

## Reporting summary

Further information on research design is available in the Nature Portfolio Reporting Summary linked to this article.

### Data availability

Raw data are available from the corresponding authors upon request. Source data are provided with this paper.

### Code availability

The computational code for image and data analysis is available via figshare at https://doi.org/10.6084/m9.figshare.22295881.v1.

## Supplementary Material

Refer to Web version on PubMed Central for supplementary material.

## Acknowledgements

This work was supported by the European Research Council (Consolidator Grant 771599 (ICEBERG) to M.T. and Advanced Grant 741773 (AAA) to L.B.), by the Bettencourt-Schueller Foundation, the Emergence program of the Ville de Paris and the Schlumberger Foundation for education and research. This project was also supported by the MuLife imaging facility, which is funded by GRAL, a program from the Chemistry Biology Health Graduate School of University Grenoble Alpes (ANR-17-EURE-0003). The work of D.M.R. and D.V. was supported by a grant from the National Institute of Health (R35GM136372). A.A. was supported by the Netherlands Organisation for Scientific Research (NWO) ECHO Grant 711.018.004. G.G. was supported by the INCA (AAP PLBIO no. 2020-109) and by the French National Research Agency (ANR-21-CE11-0004-01). M.D. was supported by the Fondation pour la Recherche Médicale (SPF201809007121).

## References

1. Heisenberg C-PP & Bellaïche Y. Forces in tissue morphogenesis and patterning. Cell 153, 948–962 (2013). [PubMed: 23706734]
2. Akhmanova A. & Kapitein LC Mechanisms of microtubule organization in differentiated animal cells. Nat. Rev. Mol. Cell Biol 23, 541–558 (2022). [PubMed: 35383336]
3. Hamant O, Inoue D, Bouchez D, Dumais J. & Mjolsness E. Are microtubules tension sensors? Nat. Commun. 10, 2360 (2019). [PubMed: 31142740]
4. Gittes F, Mickey B, Nettleton J. & Howard J. Flexural rigidity of microtubules and actin filaments measured from thermal fluctuations in shape. J. Cell Biol. 120, 923–934 (1993). [PubMed: 8432732]
5. Garzon-Coral C, Fantana HA & Howard J. A force-generating machinery maintains the spindle at the cell center during mitosis. Science 352, 1124–1127 (2016). [PubMed: 27230381]
6. Brangwynne CP et al. Microtubules can bear enhanced compressive loads in living cells because of lateral reinforcement. J. Cell Biol. 173, 733–741 (2006). [PubMed: 16754957]
7. Brouhard GJ & Rice LM Microtubule dynamics: an interplay of biochemistry and mechanics. Nat. Rev. Mol. Cell Biol. 19, 451–463 (2018). [PubMed: 29674711]
8. Akhmanova A. & Steinmetz MO Control of microtubule organization and dynamics: two ends in the limelight. Nat. Rev. Mol. Cell Biol. 16, 711–726 (2015). [PubMed: 26562752]
9. Komarova YA, Akhmanova A, Kojima SI, Galjart N. & Borisy GG Cytoplasmic linker proteins promote microtubule rescue in vivo. J. Cell Biol. 159, 589–599 (2002). [PubMed: 12446741]
10. Xu Z. et al. Microtubules acquire resistance from mechanical breakage through intralumenal acetylation. Science 356, 328–332 (2017). [PubMed: 28428427]
11. Kaverina I. et al. Tensile stress stimulates microtubule outgrowth in living cells. J. Cell Sci. 115, 2283–2291 (2002). [PubMed: 12006613]
12. Colin L. et al. Cortical tension overrides geometrical cues to orient microtubules in confined protoplasts. Proc. Natl Acad. Sci. USA 117, 32731–32738 (2020). [PubMed: 33288703]
13. Janson ME et al. Dynamic instability of microtubules is regulated by force. J. Cell Biol. 161, 1029–1034 (2003). [PubMed: 12821641]

14. Bouchet BP et al. Talin-KANK1 interaction controls the recruitment of cortical microtubule stabilizing complexes to focal adhesions. eLife 5, e18124 (2016). [PubMed: 27410476]
15. Rafiq NBM et al. A mechano-signalling network linking microtubules, myosin IIA filaments and integrin-based adhesions. Nat. Mater. 18, 638–649 (2019). [PubMed: 31114072]
16. Schaedel L. et al. Microtubules self-repair in response to mechanical stress. Nat. Mater. 14, 1156–1163 (2015). [PubMed: 26343914]
17. Aumeier C. et al. Self-repair promotes microtubule rescue. Nat. Cell Biol. 18, 1054–1064 (2016). [PubMed: 27617929]
18. Théry M. & Blanchoin L. Microtubule self-repair. Curr. Opin. Cell Biol. 68, 144–154 (2021). [PubMed: 33217636]
19. Faust U. et al. Cyclic stress at mHz frequencies aligns fibroblasts in direction of zero strain. PLoS ONE 6, e28963 (2011). [PubMed: 22194961]
20. Janke C. & Magiera MM The tubulin code and its role in controlling microtubule properties and functions. Nat. Rev. Mol. Cell Biol. 21, 307–326 (2020). [PubMed: 32107477]
21. Vasquez RJ, Howell B, Yvon AMC, Wadsworth P. & Cassimeris L. Nanomolar concentrations of nocodazole alter microtubule dynamic instability in vivo and in vitro. Mol. Biol. Cell 8, 973–985 (1997). [PubMed: 9201709]
22. Massou S. et al. Cell stretching is amplified by active actin remodelling to deform and recruit proteins in mechanosensitive structures. Nat. Cell Biol. 22, 1011–1023 (2020). [PubMed: 32719553]
23. Livne A, Bouchbinder E. & Geiger B. Cell reorientation under cyclic stretching. Nat. Commun. 5, 3938 (2014). [PubMed: 24875391]
24. Jungbauer S, Gao H, Spatz JP & Kemkemer R. Two characteristic regimes in frequency-dependent dynamic reorientation of fibroblasts on cyclically stretched substrates. Biophys. J. 95, 3470–3478 (2008). [PubMed: 18515393]
25. Bernal R, Hemelryck M, Van, Gurchenkov, B. & Cuvelier, D. Actin stress fibers response and adaptation under stretch. Int. J. Mol. Sci. 23, 5095 (2022). [PubMed: 35563485]
26. Alam SG et al. The nucleus is an intracellular propagator of tensile forces in NIH 3T3 fibroblasts. J. Cell Sci. 128, 1901–1911 (2015). [PubMed: 25908852]
27. Cadot B. et al. Nuclear movement during myotube formation is microtubule and dynein dependent and is regulated by Cdc42, Par6 and Par3. EMBO Rep. 13, 741–749 (2012). [PubMed: 22732842]
28. Jimenez AJ et al. Acto-myosin network geometry defines centrosome position. Curr. Biol. 31, 1206–1220.e5 (2021). [PubMed: 33609453]
29. Webster DR, Gundersen GG, Bulinski JC & Borisy GG Differential turnover of tyrosinated and detyrosinated microtubules. Proc. Natl Acad. Sci. USA 84, 9040–9044 (1987). [PubMed: 3321065]
30. Reid TA et al. Structural state recognition facilitates tip tracking of EB1 at growing microtubule ends. eLife 8, e48117 (2019).
31. Aher A. et al. CLASP mediates microtubule repair by restricting lattice damage and regulating tubulin incorporation. Curr. Biol. 30, 2175–2183.e6 (2020). [PubMed: 32359430]
32. Wittmann T. & Waterman-Storer CM Spatial regulation of CLASP affinity for microtubules by Rac1 and GSK3β in migrating epithelial cells. J. Cell Biol. 169, 929–939 (2005). [PubMed: 15955847]
33. Xu T. et al. SOAX: a software for quantification of 3D biopolymer networks. Sci. Rep. 5, 9081 (2015). [PubMed: 25765313]
34. Lawrence EJ, Arpag G, Norris SR & Zanic M. Human CLASP2 specifically regulates microtubule catastrophe and rescue. Mol. Biol. Cell 29, 1168–1177 (2018). [PubMed: 29540526]
35. Drabek K. et al. Role of CLASP2 in microtubule stabilization and the regulation of persistent motility. Curr. Biol. 16, 2259–2264 (2006). [PubMed: 17113391]
36. Mimori-Kiyosue Y. et al. CLASP1 and CLASP2 bind to EB1 and regulate microtubule plus-end dynamics at the cell cortex. J. Cell Biol. 168, 141–153 (2005). [PubMed: 15631994]

37. Thiam HR et al. Perinuclear Arp2/3-driven actin polymerization enables nuclear deformation to facilitate cell migration through complex environments. Nat. Commun. 7, 10997 (2016). [PubMed: 26975831]
38. Cross RA Microtubule lattice plasticity. Curr. Opin. Cell Biol. 56, 88–93 (2019). [PubMed: 30415187]
39. Webster DR & Borisy GG Microtubules are acetylated in domains that turn over slowly. J. Cell Sci. 92, 57–65 (1989). [PubMed: 2674164]
40. Ambrose C, Allard JF, Cytrynbaum EN & Wasteneys GO A CLASP-modulated cell edge barrier mechanism drives cell-wide cortical microtubule organization in *Arabidopsis*. Nat. Commun. 2, 430 (2011). [PubMed: 21847104]
41. Bouchet BP & Akhmanova A. Microtubules in 3D cell motility. J. Cell Sci. 130, 39–50 (2017). [PubMed: 28043967]
42. Wyatt TPJ et al. Actomyosin controls planarity and folding of epithelia in response to compression. Nat. Mater. 19, 109–117 (2020). [PubMed: 31451778]
43. Uchida K, Scarborough EA & Prosser BL Cardiomyocyte microtubules: control of mechanics, transport, and remodeling. Annu. Rev. Physiol. 84, 257–283 (2022). [PubMed: 34614374]
44. Robison P. et al. Detyrosinated microtubules buckle and bear load in contracting cardiomyocytes. Science 352, aaf0659 (2016).
45. Chen CY et al. Suppression of detyrosinated microtubules improves cardiomyocyte function in human heart failure. Nat. Med. 24, 1225–1233 (2018). [PubMed: 29892068]
46. Liu YJ et al. Confinement and low adhesion induce fast amoeboid migration of slow mesenchymal cells. Cell 160, 659–672 (2015). [PubMed: 25679760]
47. Delarue M. et al. Compressive stress inhibits proliferation in tumor spheroids through a volume limitation. Biophys. J. 107, 1821–1828 (2014). [PubMed: 25418163]
48. Nam S. et al. Cell cycle progression in confining microenvironments is regulated by a growth-responsive TRPV4-PI3K/Akt-p27Kip1 signaling axis. Sci. Adv. 5, eaaw6171 (2019).
49. Tse JM et al. Mechanical compression drives cancer cells toward invasive phenotype. Proc. Natl Acad. Sci. USA 109, 911–916 (2012). [PubMed: 22203958]
50. Lacroix B. et al. In situ imaging in *C. elegans* reveals developmental regulation of microtubule dynamics. Dev. Cell 29, 203–216 (2014). [PubMed: 24780738]
51. Azioune A. et al. Robust method for high-throughput surface patterning of deformable substrates. Langmuir 27, 7349–7352 (2011). [PubMed: 21604678]
52. Iguiñiz N, Frisenda R, Bratschitsch R. & Castellanos-Gomez A. Revisiting the buckling metrology method to determine the Young's modulus of 2D materials. Adv. Mater. 31, 1807150 (2019).
53. Aillaud C. et al. Evidence for new C-terminally truncated variants of α- and β-tubulins. Mol. Biol. Cell 27, 640–653 (2016). [PubMed: 26739754]
54. Ran FA et al. Genome engineering using the CRISPR-Cas9 system. Nat. Protoc. 8, 2281–2308 (2013). [PubMed: 24157548]
55. Akhmanova A. et al. CLASPs are CLIP-115 and −170 associating proteins involved in the regional regulation of microtubule dynamics in motile fibroblasts. Cell 104, 923–935 (2001). [PubMed: 11290329]
56. Chandrakar P. et al. Confinement controls the bend instability of three-dimensional active liquid crystals. Phys. Rev. Lett. 125, 257801 (2020). [PubMed: 33416339]
57. Püspöki Z, Storath M, Sage D. & Unser M. Transforms and operators for directional bioimage analysis: a survey. Adv. Anat. Embryol. Cell Biol. 219, 69–93 (2016). [PubMed: 27207363]
58. Schindelin J. et al. Fiji: an open-source platform for biological-image analysis. Nat. Methods 9, 676–682 (2012). [PubMed: 22743772]
59. Sage D, Prodanov D, Tinevez J-Y & Schindelin J. MIJ: making interoperablility between ImageJ and Matlab possible. In ImageJ User and Developer Conference 2426 (2012).
60. Tinevez J-Y et al. TrackMate: an open and extensible platform for single-particle tracking. Methods 115, 80–90 (2017). [PubMed: 27713081]
61. Mardia KV & Jupp PE Statistics of Directional Data 2nd edn (John Wiley & Sons, 2000).

62. Ruhnow F, Zwicker D. & Diez S. Tracking single particles and elongated filaments with nanometer precision. Biophys. J. 100, 2820–2828 (2011). [PubMed: 21641328]

63. Girão H. et al. CLASP2 binding to curved microtubule tips promotes flux and stabilizes kinetochore attachments. J. Cell Biol. 219, e201905080 (2020).

64. Reth M. Matching cellular dimensions with molecular sizes. Nat. Immunol. 14, 765–767 (2013). [PubMed: 23867923]

65. Mikhaylova M. et al. Resolving bundled microtubules using anti-tubulin nanobodies. Nat. Commun. 6, 7933 (2015). [PubMed: 26260773]

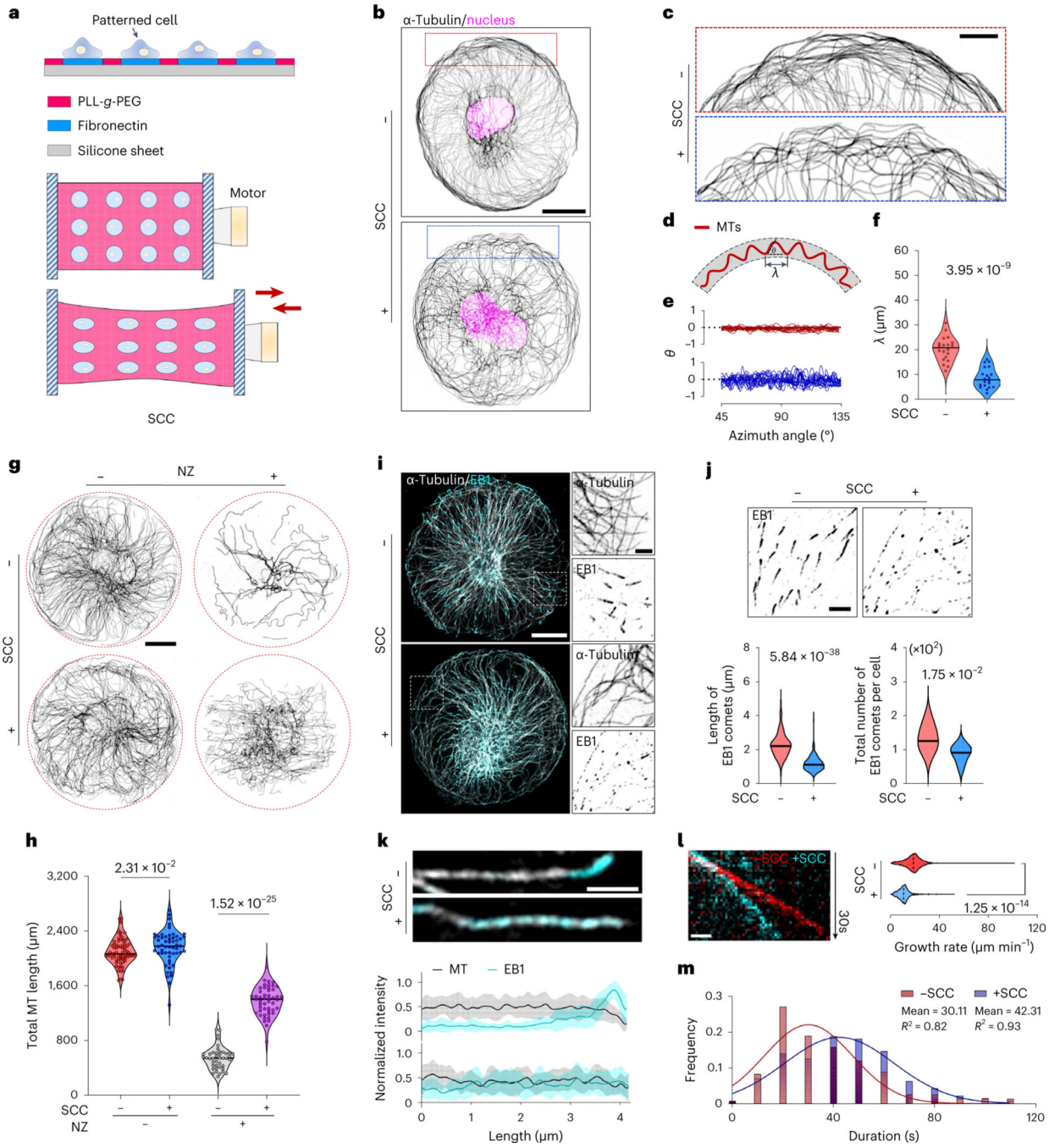


**Fig. 1 |. MTs are deformed and stabilized in response to SCC in RPE1 cells.**

**a**, Illustration of the SCC assay. **b**, Inverted IF images of micropatterned RPE1 cells with/without 10 cycles of SCC at 10% strain, stained for α-tubulin (grey) and DNA (magenta). Scale bar, 10 μm. **c**, Zoomed-in images of the MTs in peripheral regions of the representative cells in **b**. Scale bar, 5 μm. **d**, Schematic illustrating the characteristic wavelength quantification of deformed MTs. **e**, Azimuth orientation graph of MTs representing the MT waviness in cortical regions of 20 cells with/without SCC (three independent experiments). **f**, Violin plots of MT characteristic wavelength in −SCC/+SCC

conditions ($n$ = 20 cells, three independent experiments). **g**, Inverted IF images of RPE1 cells, stained for α-tubulin in varying conditions. The stretching axis is parallel to 0°. Scale bar, 10 μm. **h**, Violin plots of the total MT length of micropatterned RPE1 cells in varying conditions (−SCC/−NZ, 72 cells; +SCC/−NZ, 54 cells; −SCC/+NZ, 42 cells; +SCC/+NZ, 49 cells; three independent experiments). **i**, EB1 relocalization along MT shafts in RPE1 cells in response to SCC, stained for α-tubulin (grey) and EB1 (cyan). Scale bars, 10 μm (merged) and 2 μm (zoomed in). **j**, Inverted IF images of EB1 (top) and violin graph of the length ($n$ = 150 comets, three independent experiments) and total number ($n$ = 7 cells, three independent experiments) of EB1 comets (bottom). Scale bar, 2 μm. **k**, IF images of individual MTs and EB1 comets in cytoplasts with/without SCC (top) and the corresponding linescan profiles of normalized fluorescence intensity (bottom) ($n$ = 20 MTs from 10 cells, three independent experiments). Data are shown as mean ± s.d. Scale bar, 1 μm. **l**, Kymographs (left) and growth rate quantification of GFP-EB1 in cells with/without SCC (right) ($n$ = 994 comets, two independent experiments). Scale bar, 2 μm. **m**, Histogram of EB1 lifetime distribution with Gaussian fit functions with/without SCC ($n$ = 150 comets, three independent experiments). The panels in **i** and **k** are the representative examples of at least three independent experiments. $P < 0.05$ indicates a statistically significant difference by a two-tailed, Mann–Whitney non-parametric test. The medians are represented in the violin plots (solid line).

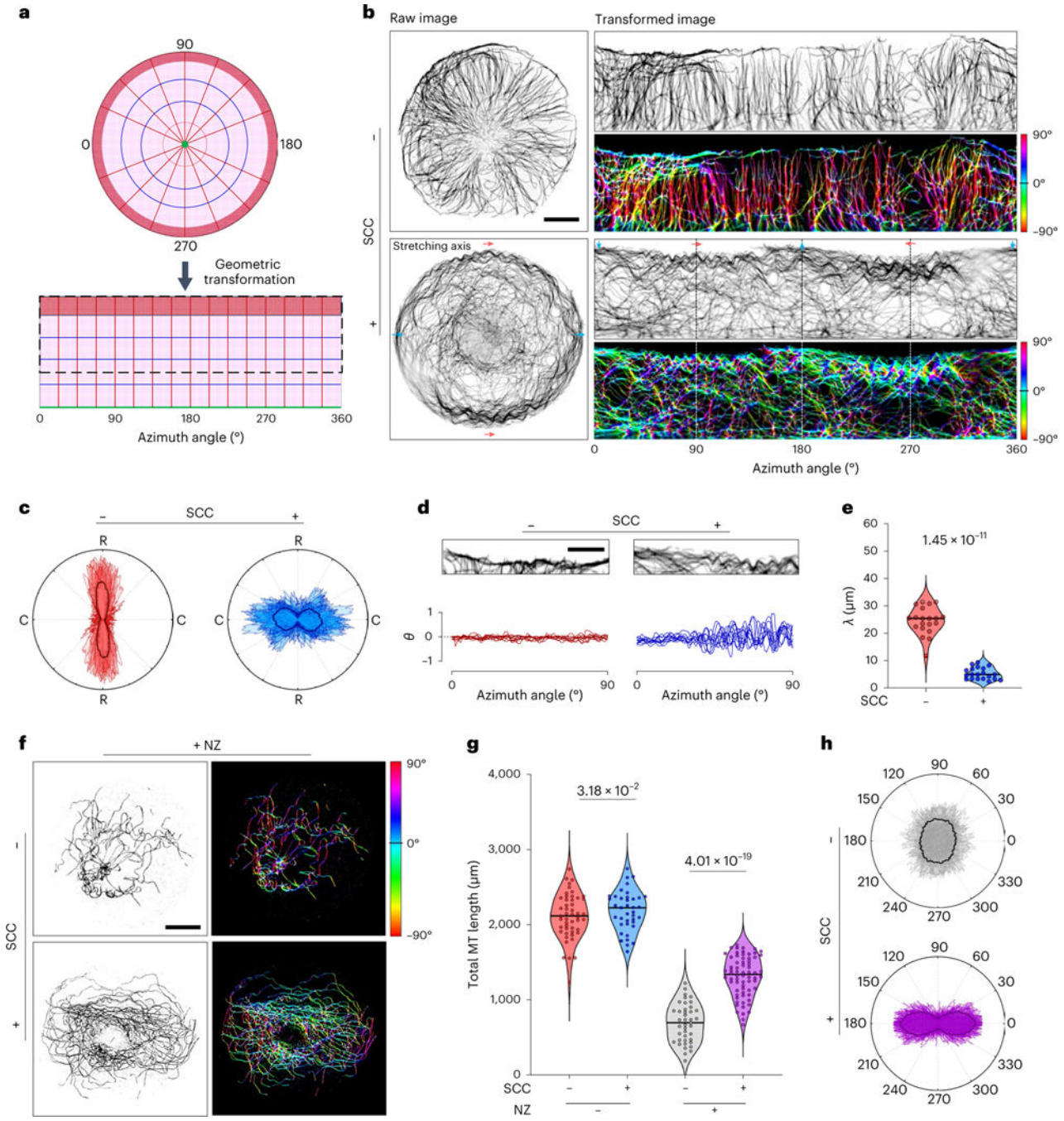


**Fig. 2 |. MTs are stabilized in response to SCC in enucleated RPE1 cells (cytoplasts).**

**a**, Illustration of geometrical transformation from a disc to a rectangular shape. The dashed box indicates the transformed region for analysis. **b**, Inverted IF images of RPE1 cytoplasts with/without SCC, stained for α-tubulin (left) and the corresponding transformed images (right). The colour-coded images indicate the local MT orientation. The arrows in IF and colour-coded images indicate the corresponding SCC axis in both raw and transformed images. Scale bar, 10 μm. **c**, Orientation polar graph of the MTs in cytoplasts in transformed images with/without SCC ($n$ = 31 cytoplasts, four independent experiments). Here R

and C represent the radial and circumferential orientation, respectively. The means are represented by the solid lines. **d**, Inverted IF images of cortical regions (azimuth angle is from 0° to 90°) of RPE1 cytoplasts with/without SCC, stained for α-tubulin (top) and the corresponding azimuth orientation analysis of MTs (bottom) that indicate the local MT waviness ($n$ = 11 cytoplasts, four independent experiments). Scale bar, 5 μm. **e**, Violin plots of MT characteristic wavelength in two conditions ($n$ = 20 cytoplasts, four independent experiments). **f**, Inverted IF images of RPE1 cytoplasts stained for α-tubulin (left) and the corresponding colour-coded orientation images in −SCC/+NZ and +SCC/+NZ conditions. Scale bar, 10 μm. **g**, Violin plots of the total MT length of micropatterned RPE1 cytoplasts in varying conditions (−SCC/−NZ, 49 cytoplasts; +SCC/−NZ, 39 cytoplasts; −SCC/+NZ, 41 cytoplasts; +SCC/+NZ, 68 cytoplasts; three independent experiments). **h**, Orientation polar graph of MTs in RPE1 cytoplasts in −SCC/+NZ and +SCC/+NZ conditions ($n$ = 20 cytoplasts, three independent experiments). The means are depicted. $P < 0.05$ indicates a statistically significant difference by a two-tailed, Mann–Whitney non-parametric test. The medians were depicted in the violin plots (solid line).

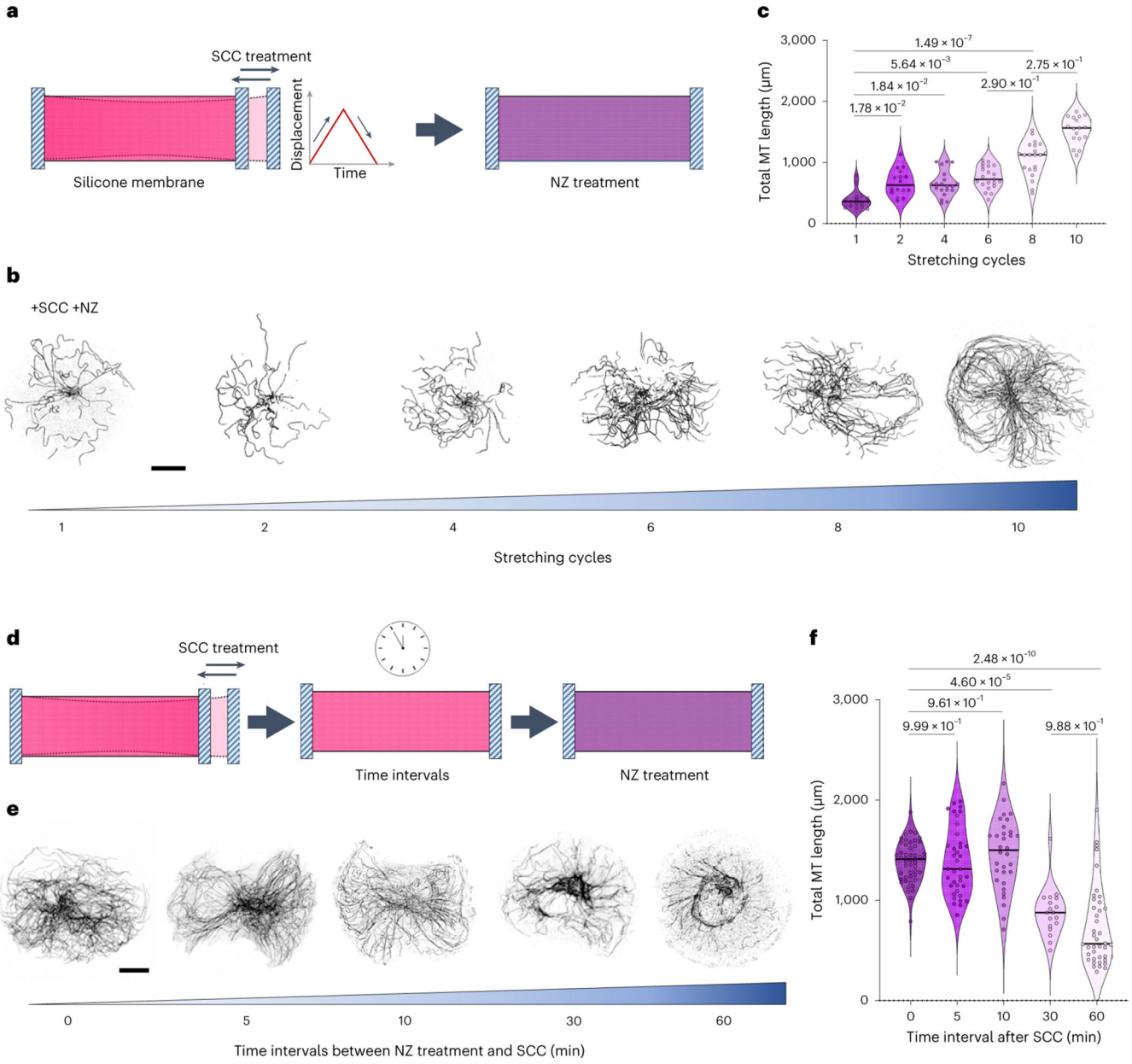


**Fig. 3 |. Characteristic timescales of MT mechano-stabilization.**

**a**, Illustration of the experimental procedure to test the effect of stretching cycles on the amount of NZ-resistant MTs in micropatterned RPE1 cytoplasts. **b**, Inverted IF images of NZ-resistant MTs in individual micropatterned RPE1 cytoplasts after different stretching cycles. Scale bar, 10 μm. **c**, Violin plots of total NZ-resistant MT length of micropatterned RPE1 cytoplasts after different stretching cycles (1 cycle, 16 cytoplasts, 2 cycles, 16 cytoplasts; 4 cycles, 20 cytoplasts; 6 cycles, 21 cytoplasts; 8 cycles, 21 cytoplasts; 10 cycles, 17 cytoplasts; three independent experiments). **d**, Illustration of the experimental procedure to test the survival time threshold of NZ-resistant MTs in micropatterned RPE1 cytoplasm after SCC treatment. **e**, Inverted IF images of NZ-resistant MTs in individual micropatterned RPE1 cytoplasts at different time intervals. Scale bar, 10 μm. **f**, Violin

plots of total NZ-resistant MT length of micropatterned RPE1 cytoplasts at different time intervals (0 min, 49 cytoplasts; 5 min, 38 cytoplasts; 10 min, 32 cytoplasts; 30 min, 18 cytoplasts; 60 min, 40 cytoplasts; three independent experiments). The panels in **b** and **e** are the representative examples of at least three independent experiments. $P < 0.05$ indicates a statistically significant difference by a Kruskal–Wallis non-parametric test with Dunn's multiple comparisons. The medians were represented in the violin plots (solid line).

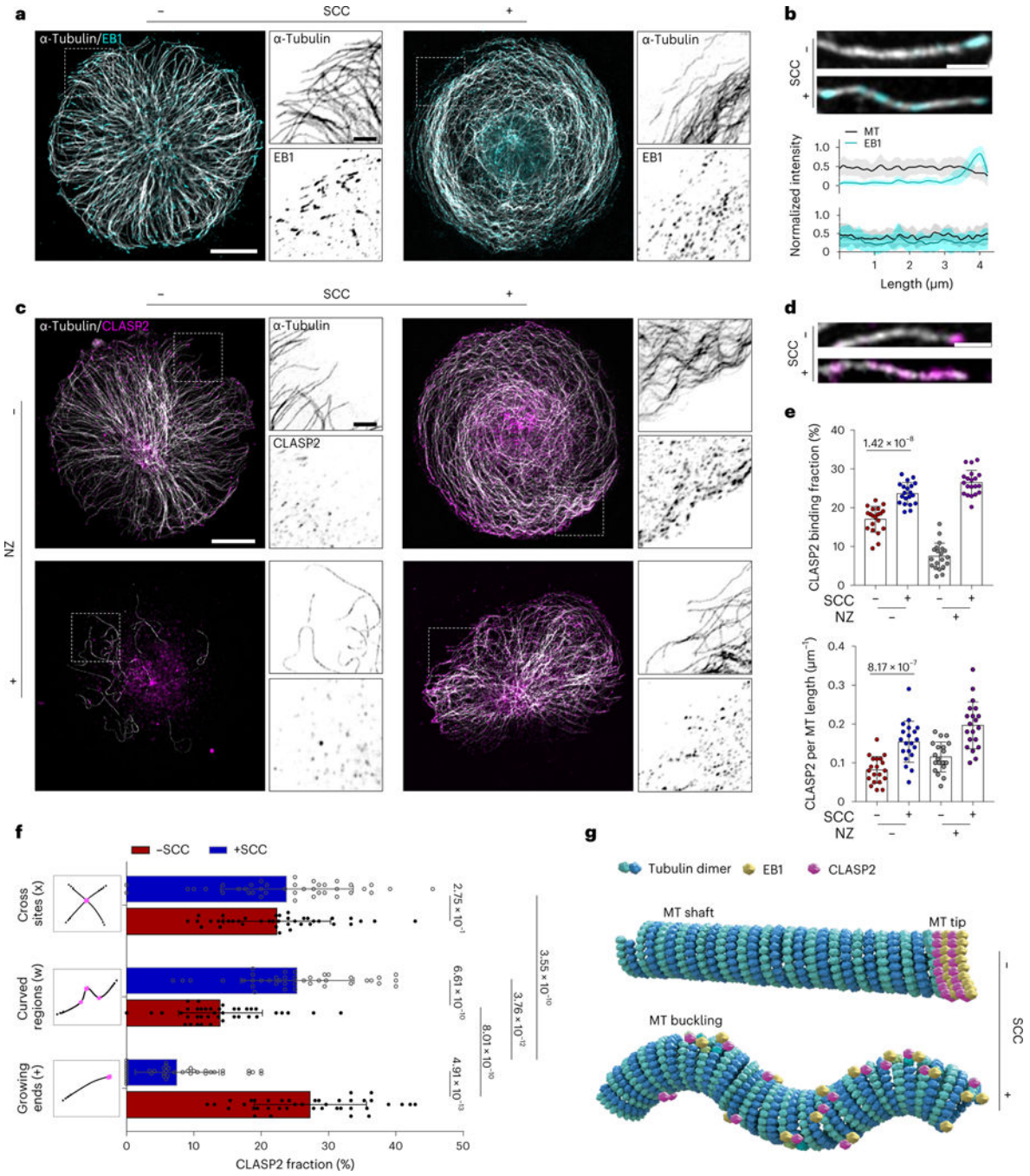


**Fig. 4 |. CLASP2 is enriched along the MT shaft in response to SCC.**

**a**, Representative IF images of RPE1 cytoplasts with/without SCC, stained for α-tubulin (grey) and EB1 (cyan). The dashed rectangle separately represents the region shown with α-tubulin or EB1 staining. Scale bars, 10 μm (merged) and 2 μm (zoomed in). **b**, Representative IF images of individual MTs and EB1 comets in cytoplasts with/without SCC (top) and the corresponding linescan profiles of normalized fluorescence intensity (bottom) ($n$ = 20 MTs from 10 cytoplasts, three independent experiments). Data are shown as mean ± s.d. Scale bar, 2 μm. **c**, IF images of RPE1 cytoplasts with/without SCC, stained for

α-tubulin (grey) and CLASP2 (magenta). The dashed rectangle designates a region shown with α-tubulin or CLASP2 channel isolated. Scale bars, 10 μm (merged) and 2 μm (zoomed in). **d**, IF images of individual MTs and CLASP2 comets in cytoplasts with/without SCC. **e**, Scatter plot of binding fraction and the number of CLASP2 along the length of MTs in four conditions ($n$ = 20 cytoplasts, three independent experiments). Data are shown as mean ± s.d. $P < 0.05$ indicates a statistically significant difference by a two-tailed, Mann–Whitney non-parametric test. **e**, Histogram of the fraction of CLASP2 binding on specific regions including growing ends, curvature peak and crossing sites of MTs (schematic illustrating the specific binding regions) ($n$ = 40 regions of interest of 10 cytoplasts, three independent experiments). Data are shown as mean ± s.d. $P < 0.05$ indicates a statistically significant difference by a Kruskal–Wallis non-parametric test with Dunn's multiple comparisons. **f**, Illustration of the relocalization of tip proteins along MT shafts in response to SCC. The panels in **a** are the representative examples of at least three independent experiments.

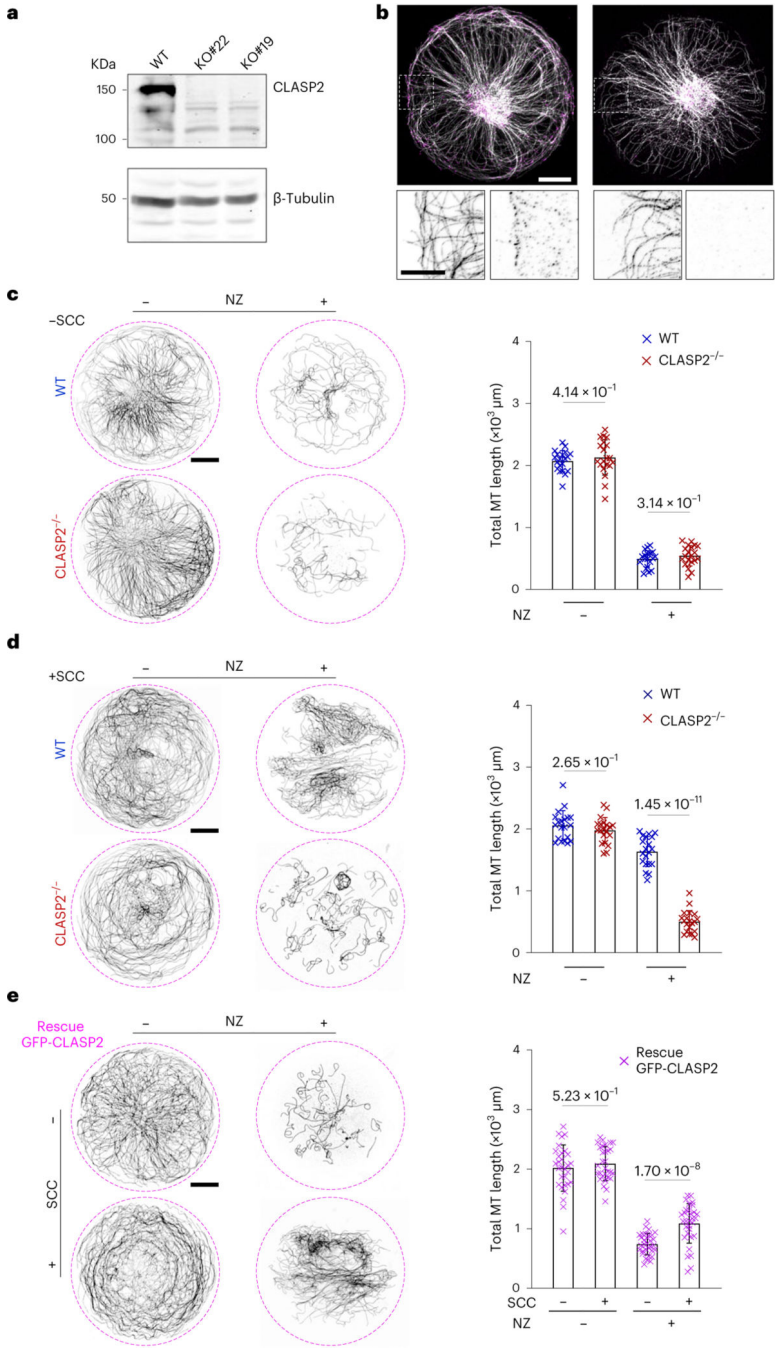


**Fig. 5 |. CLASP2 supports MT mechano-stabilization.**

**a**, CLASP2 levels of WT and KO RPE1 cells (two alleles of CLASP2 were removed using CRISPR–Cas9 (KO#22 and KO#19) and WT as control) measured by immunoblotting. **b**, IF images of WT REP1 and CLASP2 KO (CLASP2$^{-/-}$) cells stained for α-tubulin and CLASP2. The solid rectangle represents a region shown with α-tubulin or CLASP2 channel isolated. Scale bars, 10 μm (merged) and 5 μm (zoomed in). **c**, Inverted IF images of WT RPE1 and CLASP2$^{-/-}$ cytoplasts in −SCC/−NZ and −SCC/+NZ conditions. The right panel indicates the scatter plot of the total MT length in different conditions ($n$ =

20 cytoplasts, three independent experiments). Scale bar, 10 μm. **d**, Inverted IF images of WT RPE1 and CLASP2$^{-/-}$ cytoplasts in +SCC/– NZ and +SCC/+NZ conditions. The right panel indicates the scatter plot of the total MT length in different conditions ($n$ = 20 cytoplasts, three independent experiments). Scale bar, 10 μm. **e**, Inverted IF images of RPE1 cytoplasts expressed by GFP-CLASP2 stained for α-tubulin and the right panel indicates the scatter plot of the total MT length in cytoplasts. (−SCC/−NZ and +SCC/−NZ conditions, 30 cytoplasts; −SCC/+NZ and +SCC/+NZ conditions, 32 cytoplasts; three independent experiments). Scale bar, 10 μm. The panels in **a** and **b** are the representative examples of at least three independent experiments. $P < 0.05$ indicates a statistically significant difference by a two-tailed, Mann–Whitney non-parametric test. Data are shown as mean ± s.d.

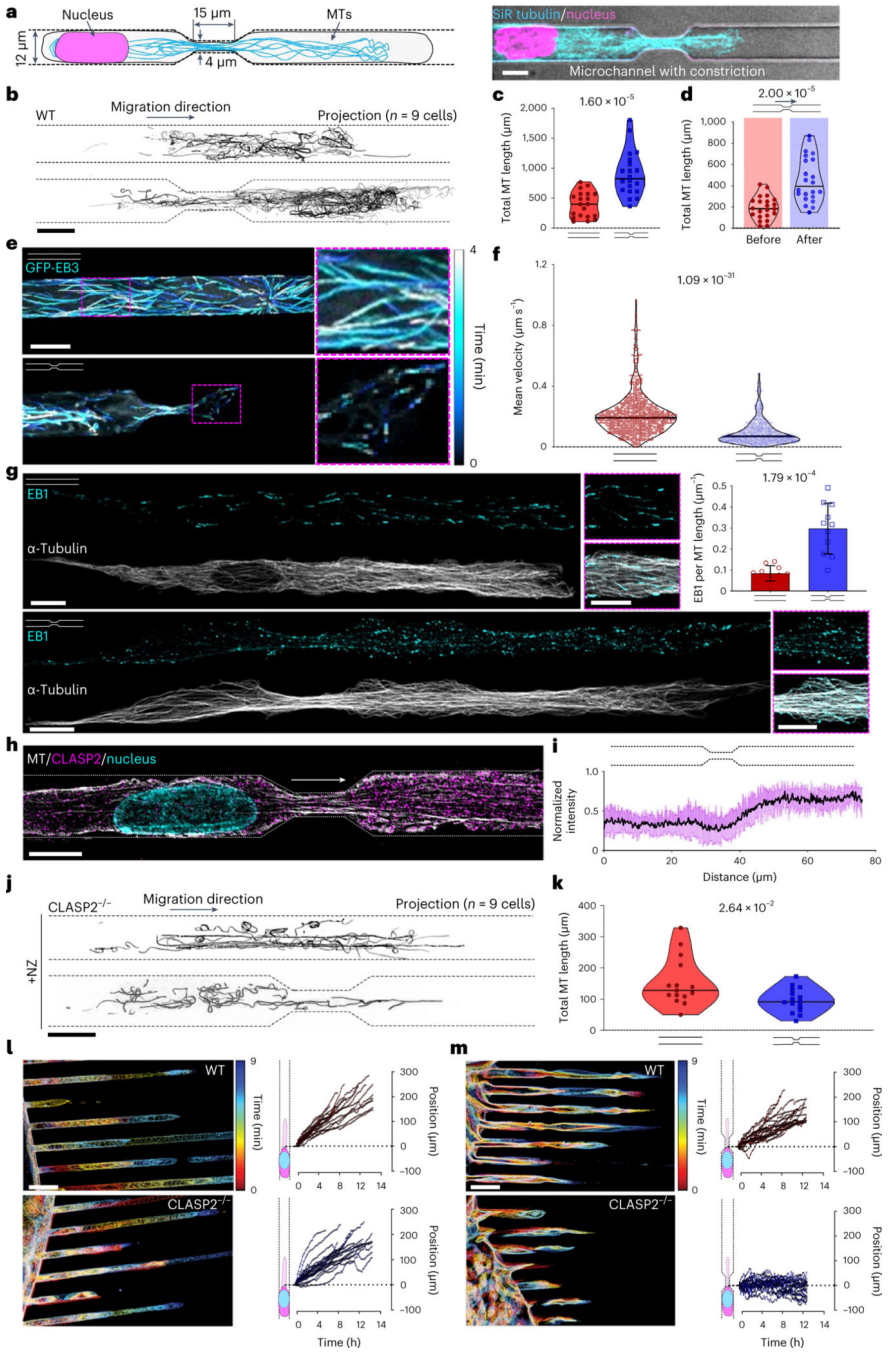


**Fig. 6 |. Cell migration through constrictions depends on the mechano-stabilization of MTs.**
**a**, Illustration of cell migration through a constriction (4 μm; left) and related IF image (right) stained for SiR-tubulin (cyan) and Hoechst (magenta) labelling. **b**, Inverted IF images of MTs after NZ treatment for WT RPE1 cells migrating through a straight channel (top) and constriction (bottom) (nine-cell projection). **c**, Violin plots of total NZ-resistant MT length for WT and CLASP2$^{-/-}$ RPE1 cells during migration ($n$ = 20 cells). **d**, Violin plots of total NZ-resistant MT length of CLASP2$^{-/-}$ RPE1 migrating cells before and after passing through the constriction ($n$ = 22 cells). **e**, Projected images of EB3–GFP RPE1

cells passing through a straight channel and constriction (period, 4 min; time interval, 1 s). **f**, Violin plots of the mean velocity of EB3 comets (826 comets for straight and 1,106 comets for constriction, tracked from 9 cells). **g**, IF images of WT RPE1 cells passing through different channels, stained for α-tubulin (grey) and EB1 (cyan). The histogram of the number of EB1 comets along the length of MTs ($n$ = 11 cells) is shown. Data are shown as mean ± s.d. **h**, IF images of WT RPE1 cell passing through a constriction, stained for α-tubulin (grey), CLASP2 (magenta) and nucleus (cyan). **i**, Corresponding linescan profiles of normalized fluorescence intensity of CLASP2 ($n$ = 11 cells). **j**, Inverted IF images of MTs after NZ treatment for CLASP2$^{-/-}$ REP1 cells migrating through a straight channel (top) and constriction (bottom) (nine-cell projection). **k**, Violin plots of total NZ-resistant MT length of CLASP2$^{-/-}$ RPE1 cells during migration ($n$ = 15 cells). **l**,**m**, Color-coded projection of SiR-tubulin-labelled WT and CLASP2$^{-/-}$ RPE1 cells migrating through the straight channel (**l**) and constriction (**m**) (left; period, 9 h; time interval, 10 min), and trajectories of the cell leading edge (right). Time 0 is when the cells are entering the straight channel or a constriction (WT, 21 cells; CLASP2$^{-/-}$, 22 cells). The samples in all the panels are examined over at least three independent experiments. Scale bars, 10 μm (**a**, **b**, **e**, **g**, **h** and **j**) and 50 μm (**l** and **m**). $P < 0.05$ indicates a statistically significant difference by a two-tailed, Mann–Whitney non-parametric test.